Theor. Comput. Fluid Dyn. (2009) 23: 63–77
DOI 10.1007/s00162-008-0089-y

ORIGINAL ARTICLE

Y. Daimon · T. L. Jackson · V. Topalian · J. B. Freund · J. Buckmaster

Effect of propellant morphology on acoustics in a planar rocket motor

Received: 7 April 2008 / Accepted: 16 October 2008 / Published online: 18 November 2008

Abstract This paper reports the results of numerical simulations of the acoustics in a two-dimensional (plane) motor using a high-order accurate, low-dissipation numerical solver. For verification we compare solutions to Culick's (AIAA J 4(8):1462–1464, 1966) asymptotic solution for constant injection, and to recent results of Hegab and Kassoy (AIAA J 44(4):812–826, 2006) for a space- and time-dependent mass injection. We present results when the injection boundary condition is described by propellant morphology and by white noise. Morphology strongly affects the amplitude of the longitudinal acoustic modes, and in this connection white noise is not a suitable surrogate.

Keywords Fluid dynamics · Acoustics · Solid rocket motor · Numerical simulations · Heterogeneous propellants

PACS 47 Fluid Dynamics and 43 Acoustics

1 Introduction

Transient sidewall mass addition (in practice, generated by propellant burning transients) can generate acoustic disturbances inside the chamber of solid rocket motors. If not properly accounted for in the design stage, resonance can occur which can lead to motor failure. Because of motor failures in past programs, the study of acoustical behavior is an old problem dating back some 50 years. For historical background and recent developments, the reader is directed to the book on combustion instability by Culick [1] and to the article by Flandro and Jacob [2]. Despite this long history of research, there are still a number of outstanding problems that are yet to be fully understood. These include an understanding of the evolution of linear disturbances into the nonlinear regime, the non-linear response for the fully coupled gas/solid combustion problem, and an understanding of the effect of propellant morphology on acoustical behavior.

Communicated by M.Y. Hussaini.

Y. Daimon · T. L. Jackson (✉)
Center for Simulation of Advanced Rockets, University of Illinois at Urbana-Champaign, Urbana, IL 61801, USA
E-mail: tlj@uiuc.edu

V. Topalian
Mechanical Science and Engineering, University of Illinois at Urbana-Champaign, Urbana, IL, USA

J. B. Freund
Mechanical Science and Engineering, Aerospace Engineering, University of Illinois at Urbana-Champaign, Urbana, IL, USA

J. Buckmaster
Buckmaster Research, Urbana, IL 61801, USA

This paper is concerned primarily with the latter question. We describe a high-order, low dissipation numerical solver, and verify it by comparisons with existing steady solutions, and existing unsteady (forced) solutions. We then use it to calculate the response when fluctuations in the injection conditions at the propellant surface are defined by two different propellants. We find that the amplitudes of the longitudinal acoustic modes are strongly influenced by the nature of the injection fluctuations, i.e., there is a significant morphology effect. In the past, absent descriptions of morphology generated fluctuations, calculations have been reported using white noise. Not surprisingly, white noise leads to longitudinal amplitudes quite different from those generated by the propellants: indeed, the amplitudes are much lower.

The paper is organized as follows. In Sect. 2 the problem formulation and the numerical method are presented. A verification study of the code is presented in Sect. 3. The verification problems include a comparison to Culick's asymptotic solution for constant injection [1], and to recent results of Hegab and Kassoy [10] for a space- and time-dependent mass injection. Section 4 presents new results when the injection boundary conditions are defined by propellant morphology for a large motor. For comparison, we also give results when white noise is used. Finally, conclusions are given in Sect. 5.

2 Formulation

We are interested in computing the acoustic modes inside a two-dimensional (plane) motor with transient sidewall mass addition. We solve numerically either the compressible Navier–Stokes (NS) equations or the equivalent parabolized Navier–Stokes equations (PNS), both written in conservative form. We use high-order accurate, low-dissipation numerical spatial and temporal schemes. More precisely, the equations are solved on a staggered mesh arrangement of variables, introduced by Harlow and Welch [3] for incompressible flows. This provides a robust formulation because of the discrete conservation of kinetic energy, mass, and momentum [4]. In addition, it provides improved resolution properties for finite-difference derivative operators [5]. A formulation for compressible flows [6] reveals superior stability properties to those of regular and collocated grid formulations. High-resolution (sixth-order) centered finite differences are used for the spatial operators. Time discretization is by a fourth-order Runge–Kutta scheme. In addition to certain Dirichlet data described below, inflow conditions, wall boundary conditions, and non-reflecting outflow conditions are implemented using the characteristics method of Poinsot and Lele [7]. Implementation of this strategy on a staggered mesh is analyzed and discussed in the PhD thesis of Topalian [8]. For all studies presented, convergence is confirmed via mesh resolution studies.

The compressible Navier–Stokes equations in nondimensional conservative form are

$$\frac{\partial U}{\partial t} + \frac{\partial F}{\partial x} + \frac{\partial G}{\partial y} = 0, \tag{1}$$

where

$$U = \begin{pmatrix} \rho \\ \rho u \\ \rho v \\ \rho e \end{pmatrix}, \quad F = \begin{pmatrix} \rho u \\ \rho u^2 + P - \dfrac{1}{Re}\tau_{xx} \\ \rho uv - \dfrac{1}{Re}\tau_{xy} \\ u(\rho e + P) - \dfrac{1}{Re}(u\tau_{xx} + v\tau_{xy}) - \dfrac{1}{\gamma - 1}\dfrac{1}{PrRe}\dfrac{\partial T}{\partial x} \end{pmatrix}, \tag{2}$$

$$G = \begin{pmatrix} \rho v \\ \rho uv - \dfrac{1}{Re}\tau_{xy} \\ \rho v^2 + P - \dfrac{1}{Re}\tau_{yy} \\ v(\rho e + P) - \dfrac{1}{Re}(u\tau_{xy} + v\tau_{yy}) - \dfrac{1}{\gamma - 1}\dfrac{1}{PrRe}\dfrac{\partial T}{\partial y} \end{pmatrix}, \tag{3}$$

with equation of state

$$\gamma P = \rho T, \tag{4}$$

and total energy defined by

$$e = \frac{P/\rho}{\gamma - 1} + \frac{1}{2}(u^2 + v^2). \tag{5}$$

In (2) and (3) the viscous stresses are proportional to

$$\tau_{xx} = 2\frac{\partial u}{\partial x} - \frac{2}{3}\left(\frac{\partial u}{\partial x} + \frac{\partial v}{\partial y}\right), \tag{6}$$

$$\tau_{xy} = \frac{\partial v}{\partial x} + \frac{\partial u}{\partial y}, \tag{7}$$

$$\tau_{yy} = 2\frac{\partial v}{\partial y} - \frac{2}{3}\left(\frac{\partial u}{\partial x} + \frac{\partial v}{\partial y}\right). \tag{8}$$

The nondimensional dependent variables are (u, v) the velocities, ρ the density, P the pressure, and T the temperature. The parabolized Navier–Stokes (PNS) equations, obtained from the Navier–Stokes equations by neglecting all viscous terms that have streamwise (x) derivatives are

$$\frac{\partial U}{\partial t} + \frac{\partial F}{\partial x} + \frac{\partial G}{\partial y} = 0, \tag{9}$$

where

$$U = \begin{pmatrix} \rho \\ \rho u \\ \rho v \\ \rho e \end{pmatrix}, \quad F = \begin{pmatrix} \rho u \\ \rho u^2 + P \\ \rho uv \\ u(\rho e + P) \end{pmatrix}, \tag{10}$$

$$G = \begin{pmatrix} \rho v \\ \rho uv - \dfrac{1}{Re}\dfrac{\partial u}{\partial y} \\ \rho v^2 + P - \dfrac{1}{Re}\dfrac{4}{3}\dfrac{\partial v}{\partial y} \\ v(\rho e + P) - \dfrac{1}{Re}(u\dfrac{\partial u}{\partial y} + \dfrac{4}{3}v\dfrac{\partial v}{\partial y}) - \dfrac{1}{\gamma - 1}\dfrac{1}{PrRe}\dfrac{\partial T}{\partial y} \end{pmatrix}. \tag{11}$$

The equations are nondimensionalized as follows: the velocities are normalized by the sound speed c_0, pressure by $\rho_0 c_0^2$, density by ρ_0, temperature by T_0, spatial coordinates by H, the channel half-height, and time by H/c_0. Here, c_0, ρ_0, and T_0 are reference values characteristic of the chamber conditions. For example, for constant and uniform injection conditions a suitable choice for T_0 is the temperature of the injected fluid. We take constant viscosity μ and constant thermal conductivity λ for convenience. The other parameters appearing in the NS and PNS equations are the Reynolds number, Re, defined as

$$Re = \frac{\mathsf{H}c_0}{\nu}, \quad \nu = \mu/\rho_0, \tag{12}$$

the Prandtl number $Pr = \mu c_p/\lambda$, and the ratio of specific heats γ. For all simulations we take $Pr = 1$. Typical values for a large motor are $\mathsf{H} = 0.1$ m, $c_0 = 10^3$ m/s, and $\nu = 10^{-4}$ m^2/s, which gives a Reynolds number on the order of $Re = 10^6$. Since the Reynolds numbers are large and the algorithm is weakly inviscidly unstable, we include a sixth-order spatial filter to keep the solution stable. Too much filtering (such as a second order filter) can significantly damp acoustic modes, but we believe that our sixth order filter does not affect the accuracy. Certainly at lower Reynolds numbers (10^4 and 10^5) solutions obtained with the filter turned off are essentially the same as those with the filter turned on. Mesh resolution studies also reveal no effect from the filtering. The computational domain (non-dimensional) is $[0, L/\mathsf{H}] \times [0, 2]$ where L is the motor length, or, when symmetry is enforced, $[0, L/\mathsf{H}] \times [0, 1]$.

Appropriate injection boundary conditions are given by

$$T = T_b(x, t), \quad \boldsymbol{n} \cdot \boldsymbol{u}_b = -v_b(x, t), \quad \text{at } y = 0, 2 \text{ for } 0 < x < \ell, \tag{13}$$

along the burning surfaces, where $\boldsymbol{n}$ is the outward normal and the non-dimensional length of the motor is $\ell = L/\mathsf{H}$. v_b is the nondimensional injection velocity (i.e., the injection Mach number) and T_b is the

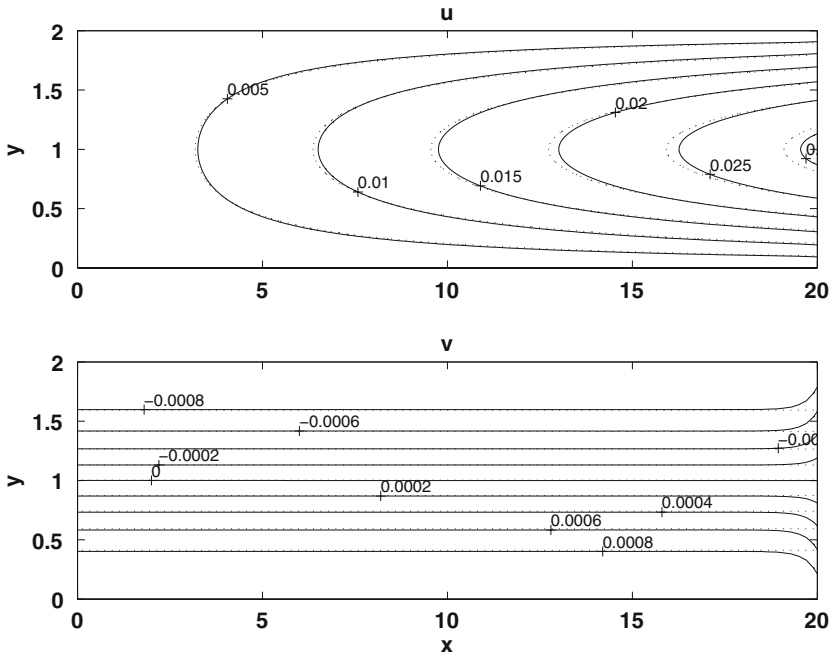

Fig. 1 Comparison of numerical solution (*solid*) with Culick's solution (*dash*) for $Re = 10^4$; u contours, *upper*, and v contours, *lower*

nondimensional injection temperature, both of which can be functions of space and time. There is no slip at the burning surface, but slip is allowed at the head-end, where also the temperature is fixed at the value 1.

It is well known that a correct description of the outflow boundary conditions is of utmost importance for the accurate prediction of thermo-acoustic instability. The outflow boundary conditions determine not only the losses of acoustic energy at the system boundary, but also the phase. Because we do not consider a nozzle in this study, we present results for the Navier–Stokes characteristic boundary conditions (NSCBC) [7].

3 Verification

For verification of the numerical solver, we first carry out numerical solutions for constant injection conditions

$$T_b = 1, \quad \boldsymbol{n} \cdot \boldsymbol{u}_b = -M_b, \tag{14}$$

where M_b is the injection Mach number, and compare the solutions to Culick's inviscid analytical solution [9] (an asymptotic solution, valid for large x), given by

$$\begin{aligned} u_s &= M_b \, \frac{\pi}{2} x \sin(\eta), \quad v_s = M_b \cos(\eta), \\ P_s &= \frac{1}{\gamma} - M_b^2 \, \frac{\pi^2}{8} \left(x^2 - \ell^2\right), \end{aligned} \tag{15}$$

where

$$\eta = \frac{\pi y}{2}. \tag{16}$$

Figures 1 and 2 show comparisons with Culick's solution for $Re = 10^4$, $\ell = 20$, and $M_b = 0.001$. The grid is $nx = 100$ and $ny = 400$ and a grid resolution study was performed to verify solution convergence. The solutions compare well with the analytical solutions except near the exit plane, a consequence of the exit-plane boundary condition. Note that there is velocity slip in the Culick solution at $x = 0$; and Culick's solution is an incompressible one, whereas ours is compressible, but the Mach number is small.

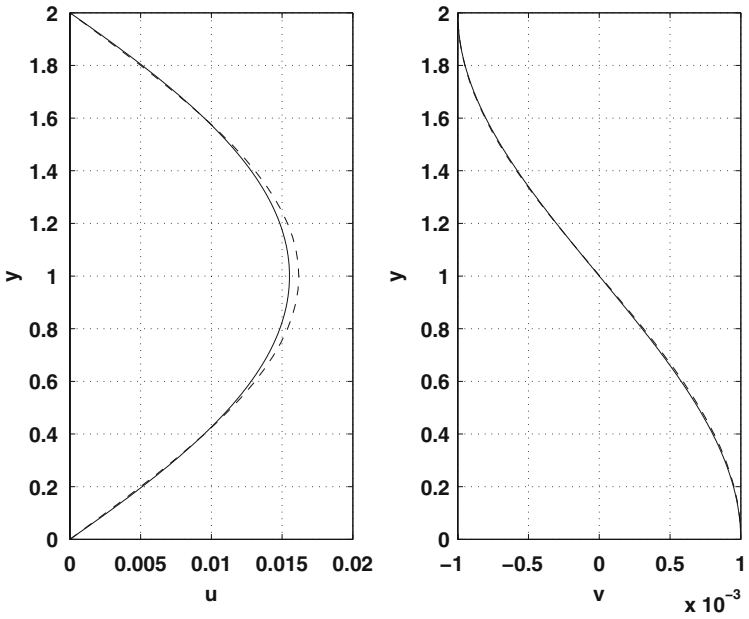

Fig. 2 Comparison of numerical solution (*solid*) with Culick's solution (*dash*) for $Re = 10^4$ at $x = \ell/2$; velocity distribution at $x = l/2$

Table 1 Parameter values from [10] and the equivalent values used in this study

Hegab & Kassoy	Current
$\omega = 1$	$\omega = 1$
$n = 1$	$n = 1$
$\epsilon = 0.4$	$\epsilon = 0.4$
$\delta = 20$	$\ell = 20$
$M = 0.02$	$M_b = 0.001$
$Re = 3 \times 10^5$	$Re = 7.5 \times 10^5$
$\gamma = 1.4$	$\gamma = 1.4$
$t = 24$	$t = 480$

For additional verification of the solver, we compare our numerical solutions with those recently published by Hegab and Kassoy [10] (hereafter HK), and we also show additional results not computed in that work. HK consider unsteady mass injection along the burning surface described by

$$T_b = 1, \quad \boldsymbol{n} \cdot \boldsymbol{u}_b = -M_b \left[1 + \epsilon \cos(\lambda_n x)(1 - \cos(\omega t/\ell))\right], \tag{17}$$

where

$$\lambda_n = \frac{n\pi}{2\ell}, \quad n = 1, 3, 5, \ldots. \tag{18}$$

Their choice of n leads to net additional mass into the chamber.

Kassoy and his co-workers have shown [11] that the disturbance vorticity field generated by the injection is the result of an inviscid interaction between the spatially distributed transient injection and the acoustic pressure gradient at the wall, itself generated by the injection. Significant vorticity is confined to a neighborhood of the wall. HK show that as n is increased from 1 to 3 to 5 this neighborhood becomes thinner, the scale of the vorticity decreases, and the magnitude of the vorticity increases. Our results duplicate those of HK (we show results for $n = 1, 5$, but not for $n = 3$, to reduce the number of figures).

Since HK use a different scaling than we do, Table 1 shows their parameter values and the corresponding values in our simulations. Note that the choice $\epsilon = 0.4$ is large enough to ensure that nonlinear effects influence the chamber flow dynamics.

Temperature contours at $t = 480$ are plotted in Figs. 3 and 4 for three different Reynolds numbers. Contours for $R = 1.5 \times 10^7$ (not shown) differ little from those for $Re = 7.5 \times 10^5$, as the inviscid limit is reached at

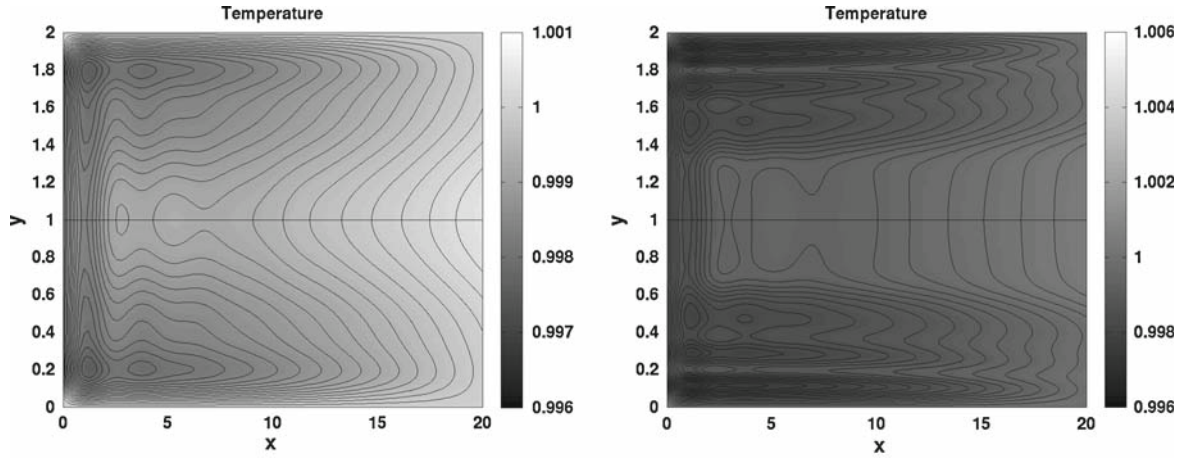

(a) $Re = 10^4$ **(b)** $Re = 10^5$

Fig. 3 Temperature contours at $t = 480$ for $Re = 10^4$ (*left*) and $Re = 10^5$ (*right*). Parameter values given in Table 1, no filtering

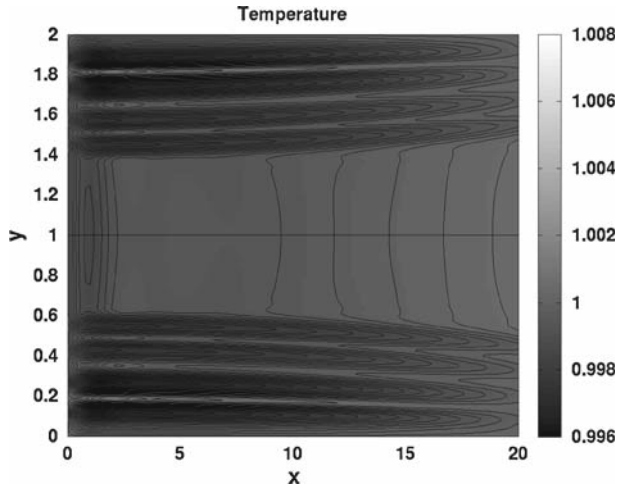

Fig. 4 Temperature contours at $t = 480$ for $Re = 7.5 \times 10^5$. Parameter values given in Table 1, filtering applied

these high Reynolds numbers. Where there is a Reynolds number effect, an increase increases the magnitude of the fluctuations near the propellant surface. Figure 4 compares well with Fig. 5a of HK.

Figure 5 shows the temperature and the temperature gradient as a function of y at $x = \ell/2$ for different values of Re. For $Re = 10^4$ and 10^5, no filtering of the solution is required because the numerical solver is stable. However, at the higher Reynolds numbers the solver becomes unstable and so the solution is filtered at the end of every time step using a sixth-order Shapiro spatial filter; the one-dimensional filter is applied in each direction separately. To ensure symmetry, the directions of the filters are alternated at each time step. Other filters give essentially the same results. When the Shapiro filter is applied at the smaller values of Re, it has negligible effect.

Resolution studies were carried out to ensure that the solutions presented here are spatially and temporally resolved, and that the stabilizing filters do not affect the solution.

The temperature and axial velocity history at $(\ell/2, 1)$ are plotted in Fig. 6 for two different frequencies, $\omega = 1$ and 1.5. For $\omega = 1$ the solution is stable and for $\omega = 1.5$ it is unstable. This plot compares well with Figs. 2 and 3 of HK, the differences being less than 1%.

The spatial variation chosen by Hegab and Kassoy, see Eq. (17) above, is not representative of spatial scales associated with composite propellants when n is assigned modest values, such as 1. They were primarily motivated to study the effects of disturbance amplitudes large enough to ensure that nonlinear effects influence the vorticity evolution within the chamber. We have shown in a previous study that the spatial microscale

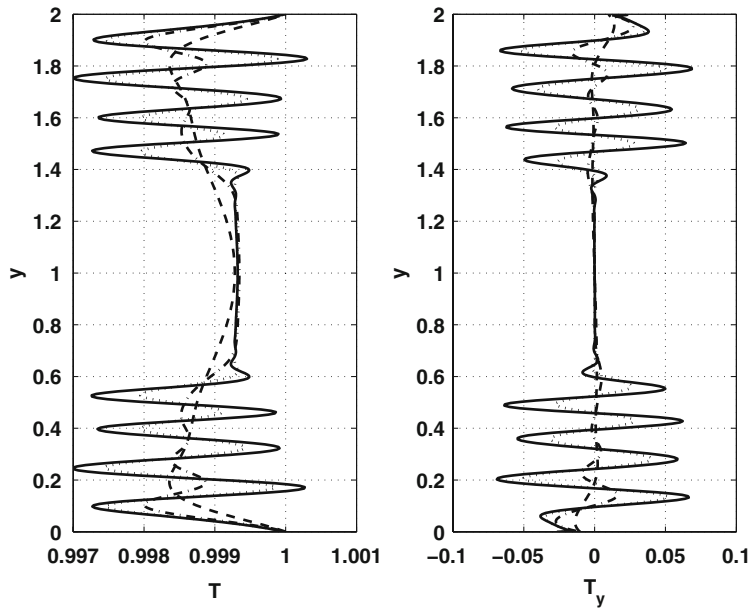

Fig. 5 Plot of the temperature (*left*) and temperature gradient (*right*) as a function of y at $x = \ell/2$ for $Re = 10^4$ (*dash*), 10^5 (*dot-dash*), 7.5×10^5 (*dot*) and 1.5×10^7 (*solid*) at $t = 480$. Parameter values given in Table 1. Corresponding temperature contours given in Figs. 3 and 4

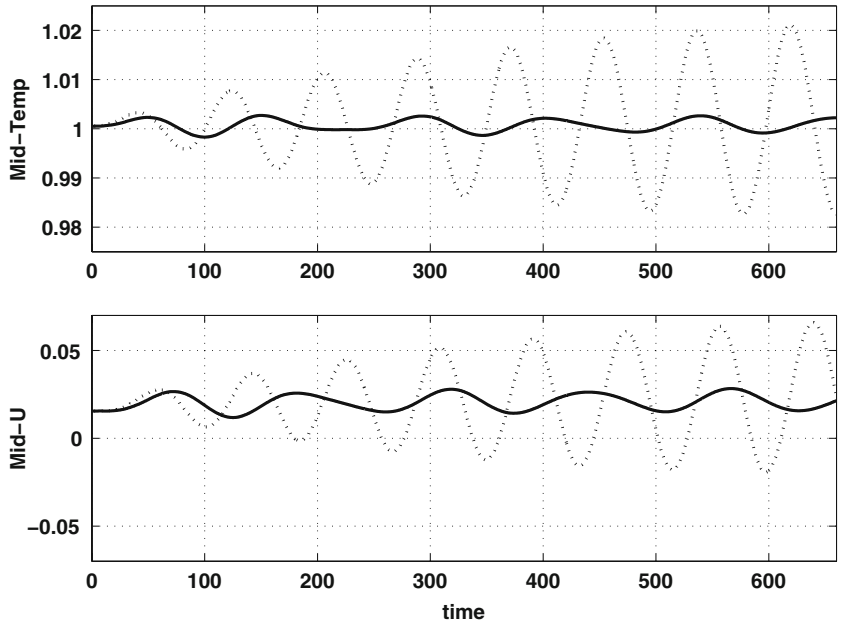

Fig. 6 Temperature and axial velocity history at $(\ell/2, 1)$ for $\omega = 1$ (*solid*) and $\omega = 1.5$ (*dash*). Parameter values given in Table 1, filtering used

associated with AP/binder propellants is on the order of a millimeter and not on the order of the length scale of the motor [12]; this corresponds to taking large values of n. Therefore we have performed an additional study by varying n between 1 and 31. Instantaneous vorticity contours at time $t = 480$ are shown in Figs. 7 and 8. For $n = 1$ and 5, the contours shown in the figures are similar to those presented in HK; new results are shown for $n = 19$ and 31. As the value of n increases, the number of mesh points in the x-direction must also be increased. The grids used for each value of n are reported in the figure captions and are selected to have a minimum of 20 mesh points inside each cosine wave along the propellant surface. The darker contour regions

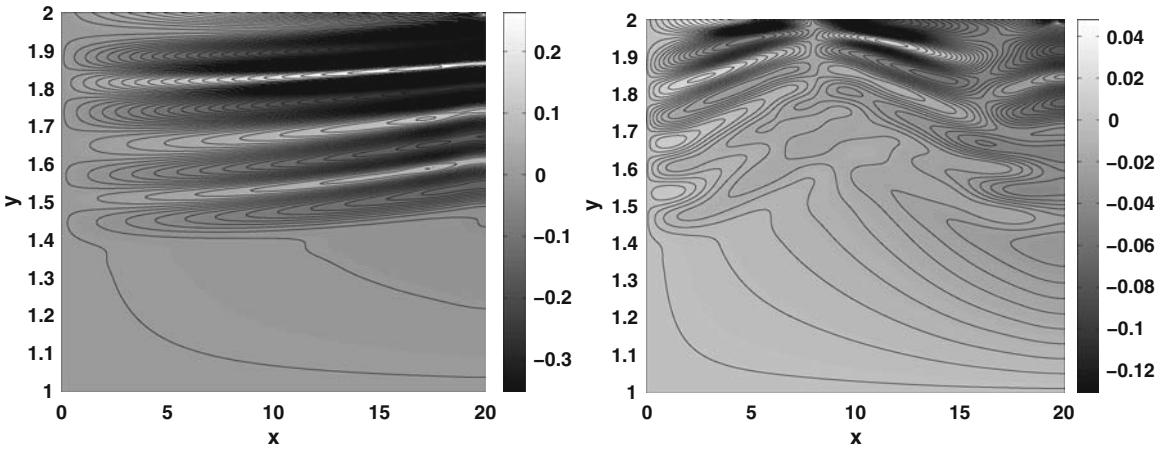

(a) $n = 1$ **(b)** $n = 5$

Fig. 7 Instantaneous vorticity contours at $t = 480$ for $n = 1$ (*left*) and $n = 5$ (*right*). The mesh has $n_x \times n_y = 80 \times 500$

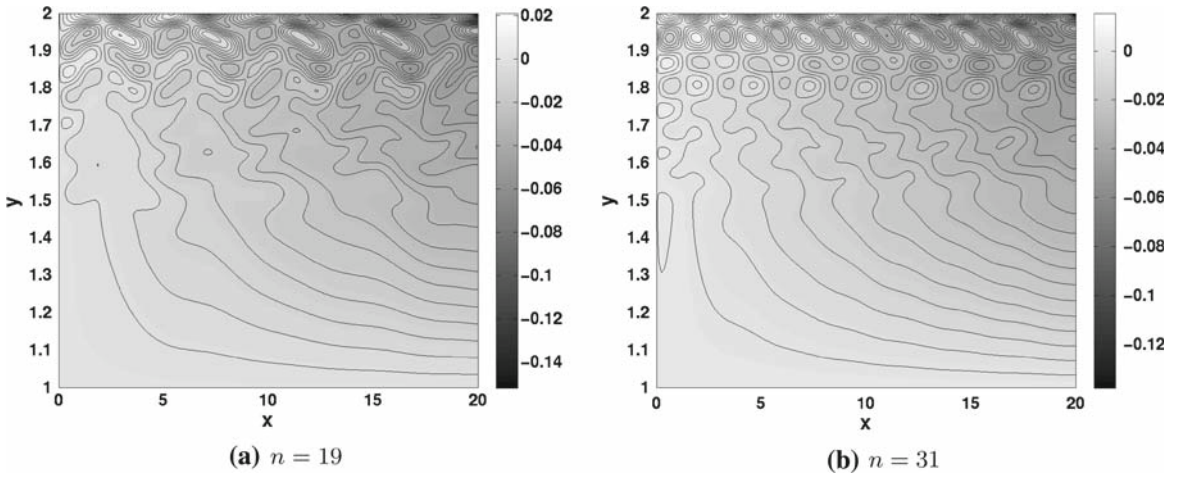

(a) $n = 19$ **(b)** $n = 31$

Fig. 8 Instantaneous vorticity contours at $t = 480$ for $n = 19$ (*left*) and $n = 31$ (*right*). The mesh has $n_x \times n_y = 80 \times 500$

correspond to large vorticity values (positive or negative), and these arise near the propellant surface. These figures show that the elongated vortical structures observed for $n = 1$ are broken up as n is increased. For $n = 31$, there are seven pairs of counter rotating vortices near the propellant surface, and these are organized. Also note that the maximum amplitude of the vorticity peaks decreases with an increase in n, consistent with the observation and analysis of HK.

HK show that for modest values of n the vortical structures can reach well into the channel region, to within 20% of the channel half-height near the centerline. In contrast, structures for larger n are confined to a region near the propellant surface.

4 Non-homogeneous injection conditions

4.1 Injection conditions defined by propellant morphology

We have recently shown numerically that the velocity-temperature correlations above a three-dimensional heterogeneous propellant are strongly influenced by the propellant morphology, which in turn can affect the amplitude of the acoustic modes inside a solid rocket motor [12]. These correlations have a spatial microscale on the order of a millimeter, and a temporal microscale on the order of a few milliseconds. Because the spatial

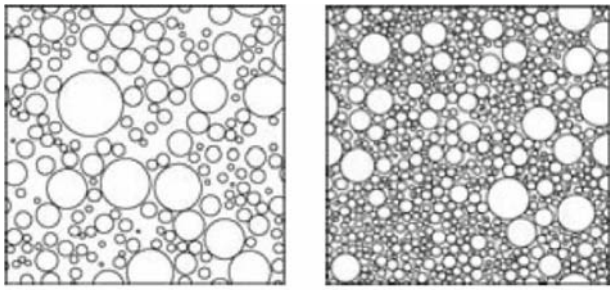

(a) TH200 **(b)** M24

Fig. 9 Cross-sectional cut of the three-dimensional packs TH200 and M24

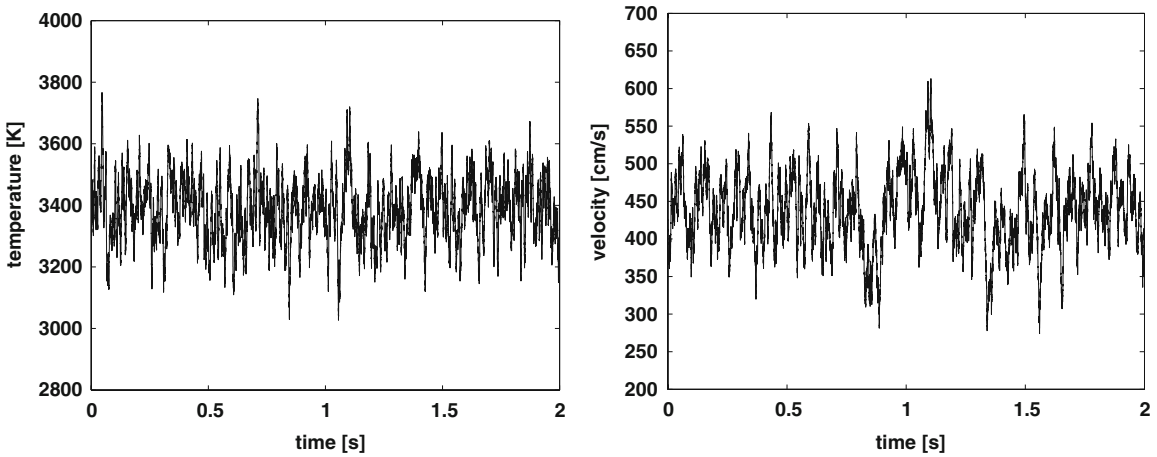

(a) TH200 **(b)** TH200

Fig. 10 Plot of the injection temperature and normal velocity as a function of time for TH200

microscale is much smaller than a typical grid, we ignore this dependence and assume the correlations are spatially independent. It does not follow, however, that just because the spatial microscale is much smaller than the mesh size these correlations have no effect on the field in the chamber. Rather, these disparate spatial scales reveal a challenging issue in the study of perturbations (including turbulence) in injection driven flows; the complete coupling between the gas phase and a heterogeneous propellant remains an unsolved problem. Assuming spatial independence, the velocity–temperature temporal correlations are described by a joint pdf, normally distributed.

In this study we investigate the acoustics inside the plane motor when the injection conditions are given by velocity-temperature temporal correlations described by two different propellant morphologies. The propellant is represented as a random pack of spheres packed in a cuboid with periodic boundary conditions. The two propellants considered here are TH200, a polydisperse 200 μm AP in an HTPB binder, and M24, a trimodal AP/HTPB propellant with 20 μm micron diameter AP for the fine, 50 μm diameter AP for the medium-size, and 200 μm diameter AP for the coarse. Figure 9 shows a cross-sectional cut of the three-dimensional packs. The injection conditions defined by TH200 are shown in Fig. 10 (see [12] for a description of how these are obtained); those for M24, not shown, are similar but not quite so varied. The PDFs are well fitted by normal distributions with mean 432.02, standard deviation 41.72 for the velocity of TH200; mean 3385.66, standard deviation 83.55 for the temperature of TH200; mean 436.16, standard deviation 52.27 for the velocity of M24; mean 3388.45, standard deviation 110.29 for the temperature of M24.

The velocity FFTs are shown in Fig. 11, and are important in comparisons with later acoustic data.

Results are shown for the plane geometry with parameters given in Table 2. Figure 12 shows the time history of the headend pressure perturbation for TH200 and M24 for a grid of 200×500. The latter was chosen following grid convergence studies, and is used throughout.

An instantaneous contour plot of spanwise vorticity is shown in Fig. 13b for $t = 1.42$ s. For comparison we show in Fig. 13a vorticity contours for the case of constant mass injection.

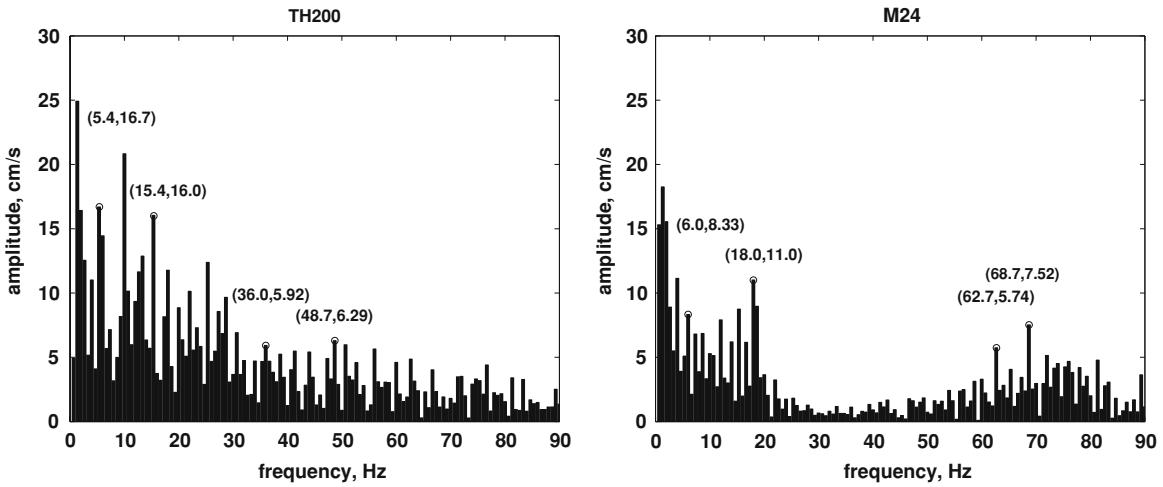

(a) TH200 **(b)** M24

Fig. 11 FFT of injection normal velocity

Table 2 Table of values for the plane motor

Parameter	Value
L (m)	35.1
H (m)	0.7
c_0 (m/s)	1037.66
V_b (m/s)	4.33
T_b (K)	3387
P (MPa)	4.053
Re	9.25×10^7

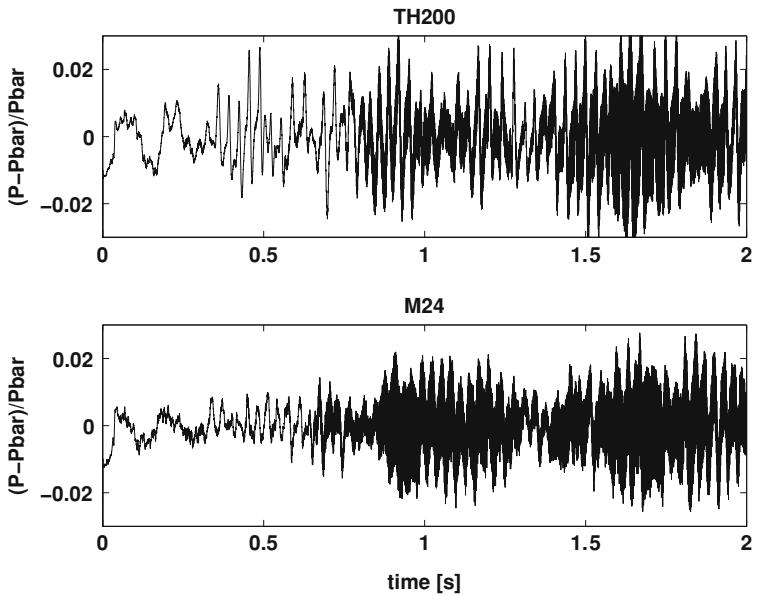

Fig. 12 Plot of the headend pressure perturbation for TH200 and M24 as a function of time for a grid of 200 × 500

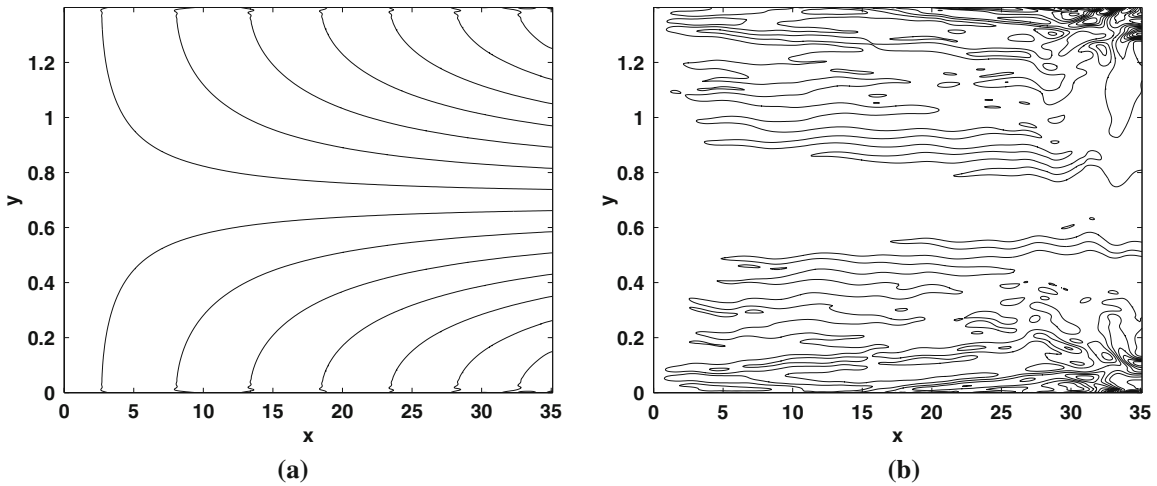

Fig. 13 Plot of spanwise vorticity for **a** constant mass injection and **b** for TH200 at $t = 1.42$ s. Grid is 200×500

Results for the pressure perturbations reveal transverse as well as axial modes, and to highlight the transverse mode we show in Fig. 14 a time sequence with interval 0.243 ms. Note that the transverse waves hit the propellant surface at $y = 1.4$ m (Fig. 14a–c), reflect (Fig. 14d), then travels towards the surface $y = 0$ (Fig. 14e–f). Similar results (not shown) are obtained for M24.

Table 3 shows the theoretical and numerical frequencies of the first six longitudinal modes, and Table 4 shows the frequencies of the first five transverse modes. The longitudinal dimensional frequencies for a closed-open tube are $f^* = mc_0/(4L)\ s^{-1}$, $m = 1, 3, 5, \ldots$, and the transverse dimensional frequencies for a closed–closed tube are $f^* = mc_0/(2H)\ s^{-1}$, $m = 1, 2, 3, \ldots$. The numerical solver is able to resolve the longitudinal modes. The fact that the high frequencies of the transverse modes compare well to those of a closed–closed tube indicates that they are not numerical noise (which would generate non-physical frequencies) but are physical.

Figure 15 shows plots of the FFTs for TH200 and M24 for low frequencies (0–90 Hz) and high frequencies (0–400 Hz), the former relevant to longitudinal modes, the latter to transverse modes. The low-frequency range is that of the propellant efflux perturbations, Fig. 11, and so the mode richness displayed in Fig. 15a and c is not surprising, and is in sharp contrast to the mode simplicity of Fig. 15b and d. However, the low frequency acoustic modes identified in Table 3 are clearly visible in (a) and (c), albeit with amplitudes that are significantly affected by the propellant morphology, Table 5. The differences are comparable to those reported in [12] for the ONERA C1 motor.

4.2 Injection Conditions Defined by White Noise

Only recently has it been possible to reasonably predict the nature of the perturbations generated in the efflux from a heterogeneous propellant, and so the default description assumes white noise. And so here we examine white noise disturbances, with PDFs the same as those of TH200. Figure 16a shows the low-frequency FFTs for the head-end pressure and here, as in the previous section, we see the first six acoustic modes, but with amplitudes an order of magnitude lower than those for heterogeneous propellants, a significant finding, we believe. The differences at high frequencies, Fig. 16b, are much less significant.

5 Conclusions

In this paper we have used a high-order, low-dissipation numerical scheme to examine disturbances in a plane rocket motor. More precisely, the configuration is rectangular (no nozzle) with a material head-end boundary, and an immaterial tail-end boundary at which outflow boundary conditions are applied. Boundary conditions appropriate for a propellant are applied at the side walls. Two verification studies are carried out. Comparisons for steady flow are made with Culick's asymptotic solution (an important example of a Taylor–Proudman flow, [13,14]), valid for large aspect ratio, and agreement is excellent except near the downstream boundary where

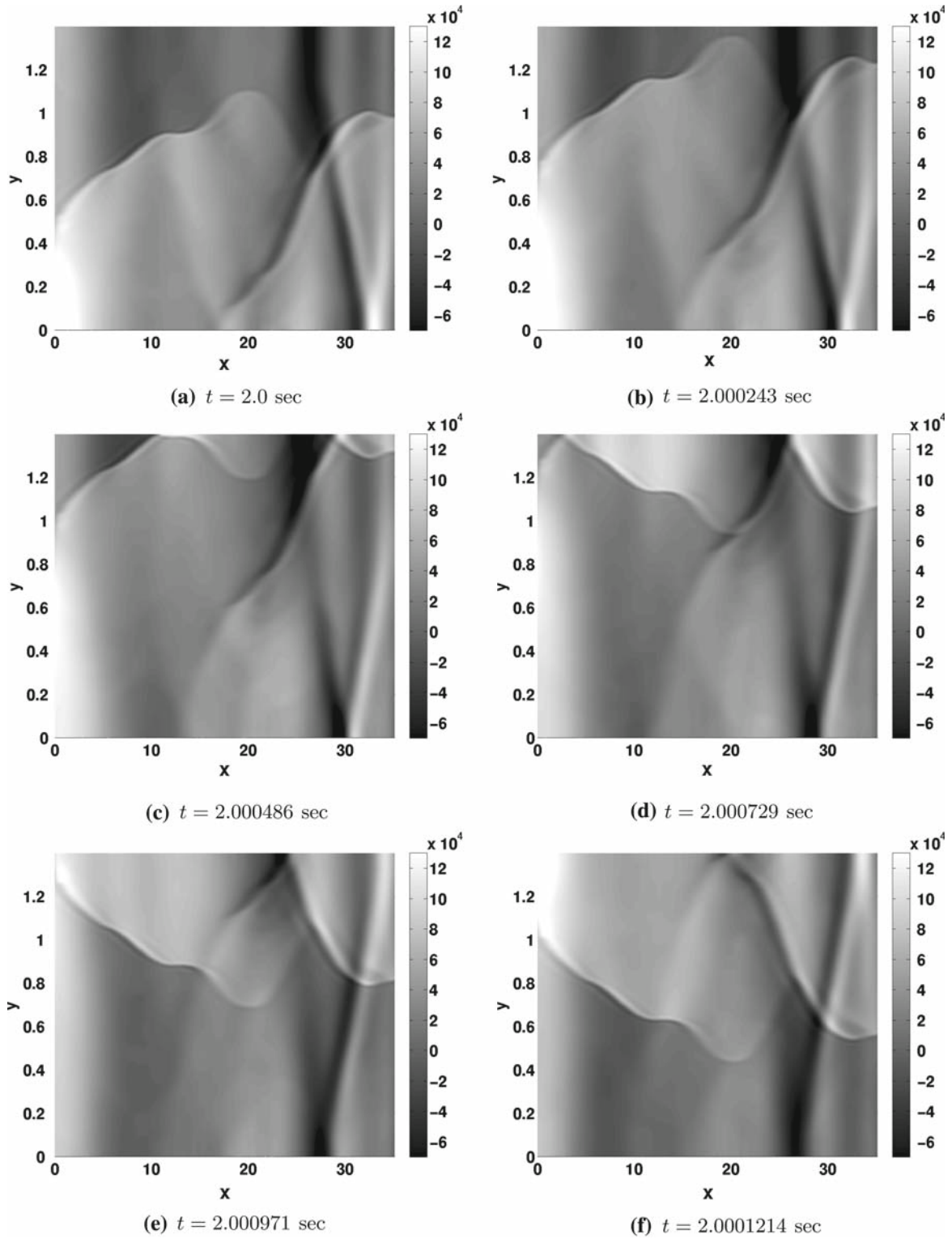

(a) $t = 2.0$ sec

(b) $t = 2.000243$ sec

(c) $t = 2.000486$ sec

(d) $t = 2.000729$ sec

(e) $t = 2.000971$ sec

(f) $t = 2.0001214$ sec

Fig. 14 Pressure perturbation contours for a time sequence with interval 0.243 ms; TH200. Grid is 200 x 500

Table 3 Theoretical and computed frequencies for longitudinal modes. Theoretical modes given by $f^* = mc_0/(4L)$, $m = 1, 3, 5, \ldots$

Longitudinal mode	1	3	5	7	9	11
Theoretical	7.39	22.17	36.95	51.74	66.52	81.30
TH200	6.65	21.4	36.0	50.7	64.0	80.7
M24	6.00	21.4	34.0	51.4	63.4	80.7

Table 4 Theoretical and computed frequencies for transverse modes. Theoretical modes given by $f^* = mc_0/(2H)$, $m = 1, 2, 3, \ldots$

Transverse mode	1	2	3	4	5
Theoretical	740.7	1481.4	2222.1	2962.9	3703.6
TH200	741	1482	2224	2965	3706
M24	739	1480	2220	2959	3705

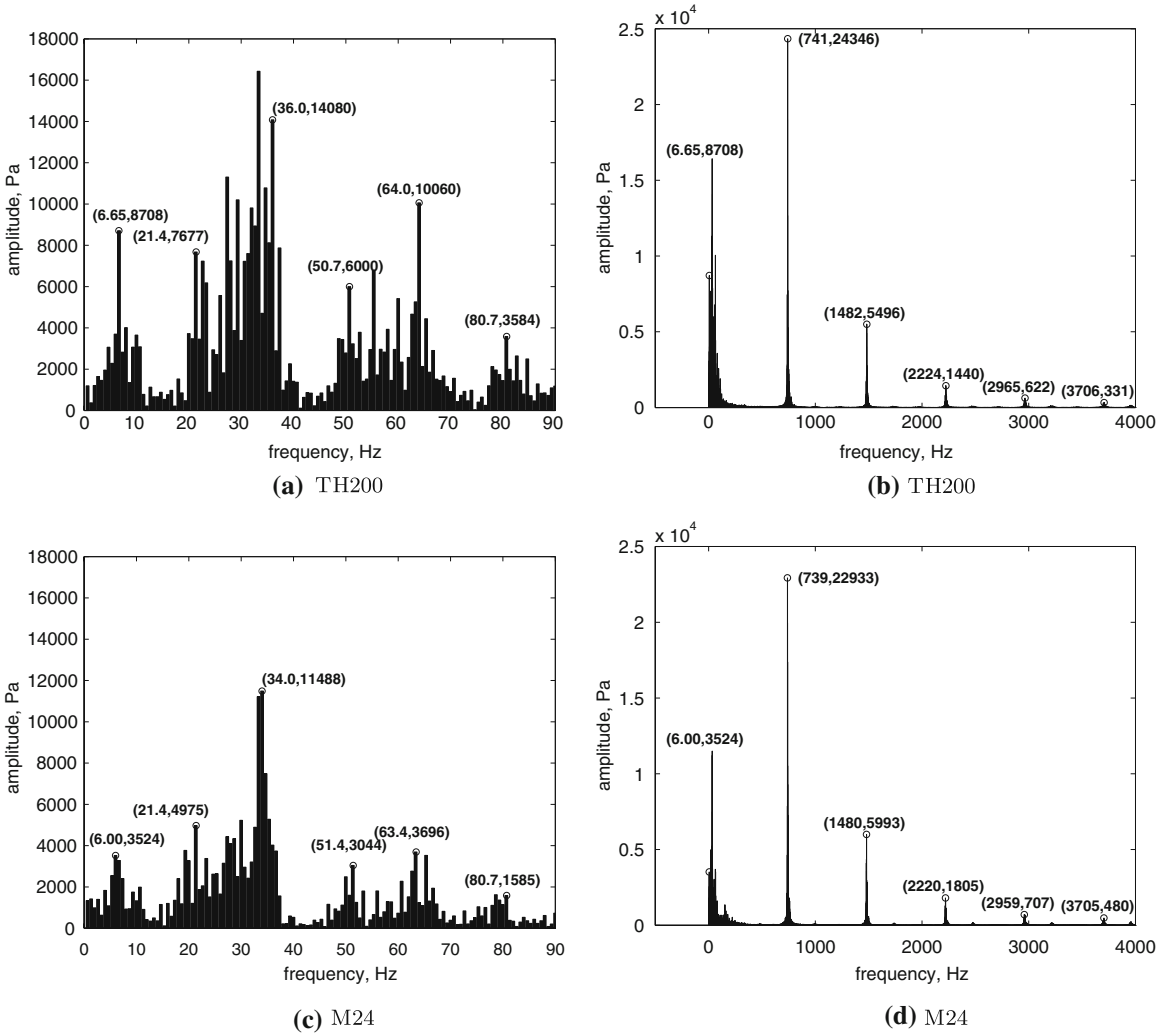

(a) TH200 **(b)** TH200

(c) M24 **(d)** M24

Fig. 15 Plot of FFTs for TH200 (*top*) and M24 (*bottom*) over the time interval [0.5, 2.0] s

our solutions are influenced by the outflow conditions. Unsteady solutions generated by a propellant velocity efflux that is periodic in space and time are compared with solutions generated by Hegab and Kassoy [10], with good agreement. Motivated by the fact that the combustion of heterogeneous propellants introduces short wavelength fluctuations, we have extended the Hegab–Kassoy problem to wavelengths shorter than those that

Table 5 Computed amplitudes (in Pa) for TH200 and M24, and their relative difference in percent

TH200	M24	(TH200-M24)/TH200 (%)
8,708	3,524	59.5
7,677	4,975	35.2
14,080	11,488	18.4
6,000	3,044	49.3
10,060	3,696	63.3
3,584	1,585	55.8

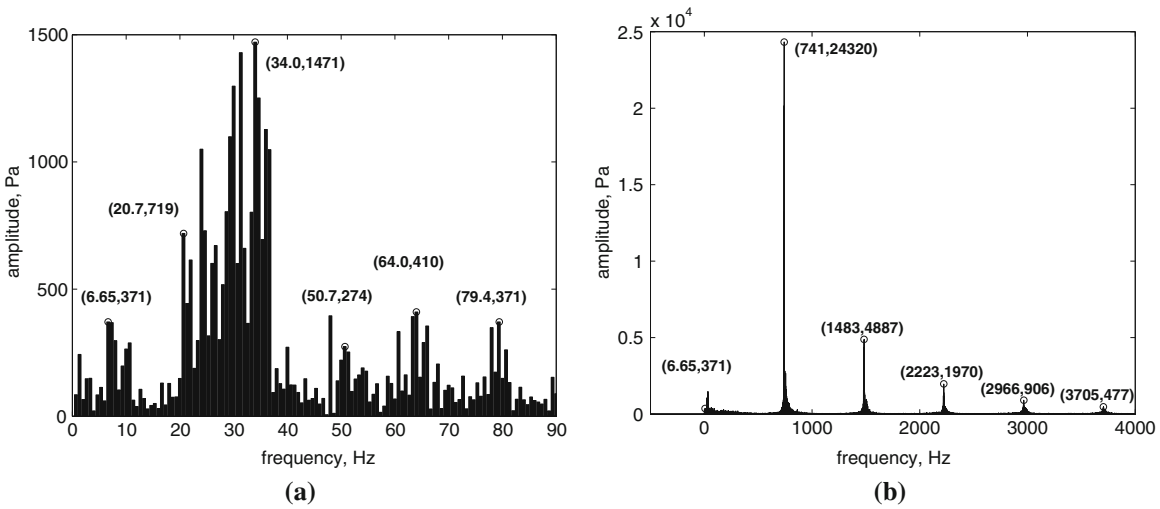

Fig. 16 FFT of white noise. **a** Low frequencies and **b** high frequencies

they examined, and find (just as HK do for n up to 5) that as the wavelength is decreased the vortical structures are broken up, the maximum vorticity decreases, and the vortical structures move closer to the side walls. It is tempting to assume that as the wavelength approaches zero (i.e., the wave-number, n, approaches infinity) the vortical structures disappear, and the solutions are those for $n = 0$. Tempting, because the length scales defined by propellant morphology are subgrid. However, that which is tempting is not necessarily real, and the full flow interaction with these small scales is presently an unsolved problem.

The truly new calculations in the paper are for heterogeneous propellants. For the reasons stated in the preceding paragraph we do not allow for fluctuation length scales, but we do allow for time scales, scales identified in previous work on propellant combustion [12]. We consider two quite different propellants, characterized by the packing of AP spheres of various sizes in a matrix of HTPB, and we also consider a propellant in which it is assumed that the fluctuations can be defined by white noise. A notable characteristic of the solutions are highly irregular transverse mode structures. Key quantitative results are defined by an examination of the FFT of the head-end pressure, and the comparison between this and the FFT of the fluctuations. In this connection we make a distinction between low frequency modes (0–90 Hz) and high frequency modes (0–400 Hz). For the parameters we have chosen for these calculations the important longitudinal acoustic modes are low frequency, whereas the important acoustic transverse modes are high frequency.

The propellant fluctuations are low frequency, and the low frequency range of the head-pressure FFT shows these fluctuations, together with the longitudinal modes. The amplitudes of the latter are quite different for the two "real" propellants, a significant morphology effect. The high frequency range of the head-pressure FFT consists essentially of the transverse acoustic modes. When white noise is used, instead of the well-defined morphology generated fluctuations, the head-end pressure FFT is qualitatively similar, but the amplitude of the longitudinal acoustic modes are much smaller. In other words, white noise is not a surrogate for actual morphology generated fluctuations.

Acknowledgments This work was supported by the US Department of Energy through the University of California under subcontract number B523819; and by the Air Force Research Laboratory under contract FA9550-06-C-0078, program manager Dr. A. Nachman.

References

1. Culick, F.E.C.: Unsteady motions in combustion chambers for propulsion systems. RTO AGARDograph, AG-AVT-039 (2006)
2. Flandro, G.A., Jacob, E.: Finite amplitude waves in liquid rocket combustion chambers. AIAA Paper 2008-1003. 46th AIAA Aerospace Sciences Meeting and Exhibit, Reno, Nevada, January 7–10 (2008)
3. Harlow, F.H., Welch, J.E.: Numerical calculation of time-dependent viscous incompressible flow of fluid with free surface. Phys. Fluids **8**, 2182 (1965)
4. Moronishi, Y., Lund, T.S., Vasilyev, O.V., Moin, P.: Fully conservative higher order finite difference schemes for incompressible flow. J. Comput. Phys. **143**(1), 90–124 (1998)
5. Lele, S.K.: Compact finite difference schemes with spectral-like resolution. Comput. Phys. **103**(1), 16–42 (1992)
6. Nagarajan, S., Lele, S.K., Ferziger, J.H.: A robust high-order compact method for large eddy simulation. J. Comput. Phys. **191**(2), 392–419 (2003)
7. Poinsot, T.J., Lele, S.K.: Boundary conditions for direct simulations of compressible viscous flows. J. Comput. Phys. **101**, 104–129 (1992)
8. Topalian, V.: UIUC PhD thesis, in preparation (2008)
9. Culick, F.E.C.: Rotational axisymmetric mean flow and damping of acoustic waves in a solid propellant rocket. AIAA J. **4**(8), 1462–1464 (1966)
10. Hegab, A.M., Kassoy, D.R.: Internal flow temperature and vorticity dynamics due to transient mass addition. AIAA J. **44**(4), 812–826 (2006)
11. Zhao, Q., Staab, P.L., Kassoy, D.R., Kirkkopru, K.: Acoustically generated vorticity in an internal flow. J. Fluid Mech. **413**, 247–285 (2000)
12. Massa, L., Jackson, T.L., Buckmaster, J., Najjar, F.: Fluctuations above a burning heterogeneous propellant. J. Fluid Mech. **581**, 1–32 (2007)
13. Taylor, G.I.: Fluid flow in regions bounded by porous surfaces. Proc. R. Soc. Lond. A **234**, 456–475 (1956)
14. Proudman, I.: An example of steady laminar flow at large Reynolds number. J. Fluid Mech. **9**, 593–602 (1960)